



Oriented $Zn_mIn_2S_{m+3} @ In_2S_3$ heterojunction with hierarchical structure for efficient photocatalytic hydrogen evolution

Yuxiang Li^{a,*}, Ping Han^{a,1}, Yali Hou^{a,1}, Shaoqin Peng^a, Xiaojun Kuang^{b,*}

^a Department of Chemistry, Nanchang University, Nanchang 330031, PR China

^b College of Materials Science and Engineering, Guilin University of Technology, Guilin 541004, PR China



ARTICLE INFO

Keywords:

$Zn_mIn_2S_{m+3}$
 In_2S_3
Oriented
Heterojunctions
Hierarchical
Structures
Oxalic acid

ABSTRACT

It remains a great challenge to design and prepare highly efficient semiconductor-based photocatalysts for water splitting. To achieve this goal, the design of oriented heterojunctions for efficient carrier transport and separation is a new strategy based on their conductive anisotropy. Herein, a novel oriented J-J type $Zn_mIn_2S_{m+3} @ In_2S_3$ heterojunction photocatalyst with hierarchical structures is fabricated with the assistance of oxalic acid. The hierarchical structures consist of ‘flower-like’ hollow $Zn_mIn_2S_{m+3}$ microspheres with epitaxially grown quantum confined In_2S_3 along the petal rims (J-J type heterojunction). This heterojunction improves the transport and separation of the photoexcited carriers, and extends the visible-light response range. Thus, the heterojunction photocatalyst exhibits significantly enhanced photocatalytic activity with a hydrogen evolution rate of $330 \mu\text{mol h}^{-1}$, which is about 4 times higher than that of single $ZnIn_2S_4$. The findings provide new insights to construct efficient oriented heterojunctions for anisotropic semiconductors.

1. Introduction

Due to the global energy crisis and environmental pollution, photocatalytic water splitting into clean H_2 fuel has attracted considerable attention [1–12]. Ternary chalcogenide $ZnIn_2S_4$ with a layered hexagonal structure is an attractive photocatalyst because of suitable band gap (2.34–2.48 eV) for visible light response, and proper conduction band position for H_2O reduction into H_2 [13–24]. $Zn_mIn_2S_{3+m}$ ($m = 2–5$) also shows photocatalytic activity for hydrogen evolution [25,26]. Although $Zn_mIn_2S_{3+m}$ ($m = 1–5$) compounds change in composition, they adopt similar layer structures consisting of alternative tetrahedral Zn, octahedral In and tetrahedral In layers isolated by vacant cationic layers (Scheme 1a–b).

However, owing to the rapid recombination and low efficient transport of photoexcited electron-hole pairs, the photoactivity of $Zn_mIn_2S_{m+3}$ alone is limited. Constructing $ZnIn_2S_4$ -based heterojunctions with other suitable semiconductors has been evidenced to be an effective strategy to enhance the efficiency of carrier transfer and separation, and photocatalytic activity [28–36]. Since the electrical conductivity of layered $ZnIn_2S_4/Zn_mIn_2S_{m+3}$ semiconductor is anisotropic (the resistance along the c axis is much greater than that along the ab plane due to the anisotropic structure and composition defects) [26,37], the carrier separation efficiency of the oriented J-type

heterojunction along the ab plane should be much higher than that of the H-type one along the c axis (Scheme 1c). Recently, we successfully fabricated a unidirectional J type $ZnIn_2S_4 @ In(OH)_3$ heterojunction, and found that the J type heterojunction greatly enhances the photocatalytic activity compared to single $ZnIn_2S_4$, while the H type one does not [38]. Because $In(OH)_3$ cannot absorb visible light ($E_g = 5.17$ eV), to extend the absorption range of the heterojunction, it is highly desirable to couple $ZnIn_2S_4$ with narrow semiconductors such as In_2S_3 ($E_g = 2.0–2.2$ eV) [39].

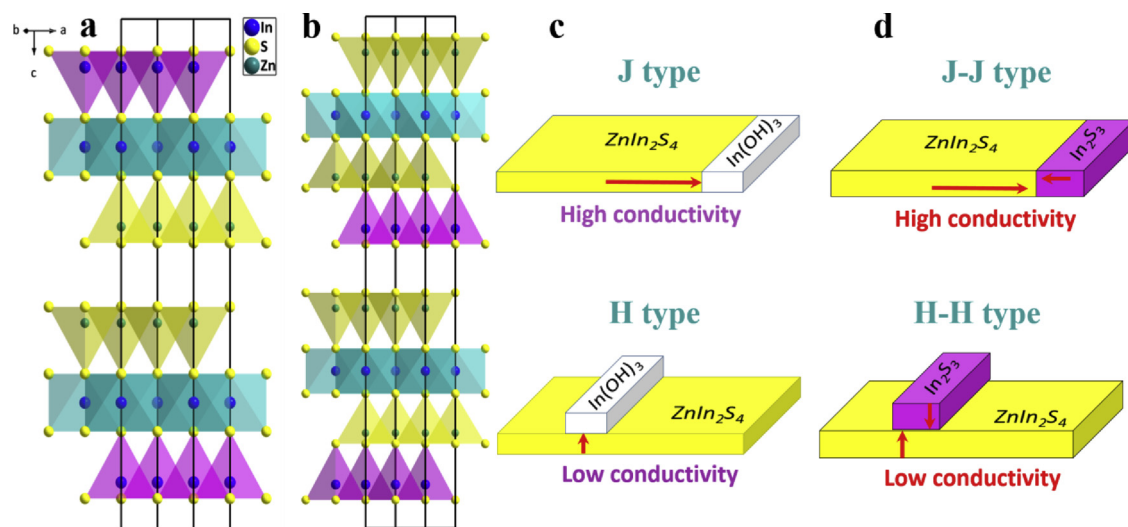
The conductivity of both tetragonal and hexagonal In_2S_3 is also anisotropic [40]. The conductivity of the layered hexagonal In_2S_3 in basal plane should be higher than that in the perpendicular direction owing to the energy barrier from its layered stacking disorder [26]. If both the hexagonal In_2S_3 and $ZnIn_2S_4/Zn_mIn_2S_{m+3}$ sheets link in J-J type mode to construct an oriented heterojunction, that is, the epitaxial growth of In_2S_3 along the plane of $Zn_mIn_2S_{m+3}$, the efficiency of the bidirectional carriers transport and separation of the heterojunction should be highly efficient compared to the H-H one (Scheme 1d).

To achieve epitaxial growth of In_2S_3 sheets along the plane of $Zn_mIn_2S_{m+3}$ (J-J type) rather than spontaneous growth on the sheet (H-H type), the homogeneous nucleation of In_2S_3 should be avoided at high supersaturation. The heterogeneous nucleation of In_2S_3 monomers at low supersaturation is beneficial to build the J-J type heterojunction. In

* Corresponding authors.

E-mail addresses: liyx@ncu.edu.cn (Y. Li), kuangxj@glut.edu.cn (X. Kuang).

¹ These authors contributed equally to this work.



Scheme 1. Crystal structures for the homogeneous hexagonal $Zn_mIn_2S_{3+m}$ viewed toward the (010) plane: (a) $m = 1$, (b) $m = 2$; (c) Schematic illustration of two unidirectional heterojunctions of $ZnIn_2S_4@In(OH)_3$ (J and H types) based on the anisotropic conductivity of $ZnIn_2S_4$ alone; (d) Schematic illustration of two oriental heterojunctions of $ZnIn_2S_4@In_2S_3$ (J-J and H-H types) for the bidirectional transport of the carriers based on their anisotropic conductivity.

principle, the decrease of the supersaturation can be realized via reducing free In^{3+} or/and S^{2-} concentration.

Herein, we develop a novel method to construct J-J type $Zn_mIn_2S_{m+3}@In_2S_3$ heterojunction with the assistance of oxalic acid. Oxalic acid acts not only as a ligand and precipitant to form $In(C_2O_4)_{3-2x}$ complex and $In_2(C_2O_4)_3$ precipitate [41], respectively, but also as the provider of H^+ ions, leading to very low free In^{3+} and S^{2-} concentrations. In this case, the early formed $Zn_mIn_2S_{m+3}$ sheet rims as heterogeneous crystal nuclei promote the oriented growth of J-J type $Zn_mIn_2S_{m+3}@In_2S_3$ heterojunction with ‘flower-like’ hierarchical structure. This heterojunction improves the carrier separation efficiency and extends the visible-light response range. Thus, the heterojunction photocatalyst shows highly efficient photocatalytic H_2 evolution under visible light irradiation. The findings provide new insights to construct efficient oriented heterojunctions for anisotropic semiconductors.

2. Experimental

2.1. Preparation of photocatalysts

All chemicals with analytic grade were used without further purification. The J-J type $Zn_mIn_2S_{m+3}@In_2S_3$ heterojunction was prepared via a hydrothermal method with the assistance of oxalic acid. In a typical synthesis process, $ZnCl_2$ (1.0 mmol), $In_2(SO_4)_3 \cdot 6H_2O$ (1.0 mmol) and excess thioacetamide (TAA, 4.8 mmol) were sequentially dissolved in 60 mL of distilled water to obtain a clear solution. Next, 2.0 mmol of oxalic acid ($H_2C_2O_4 \cdot 2H_2O$) was added and dissolved in the solution in 2 min under stirring to obtain a clear solution. The solution turned cloudy after 0.5 h stirring, and a white precipitate was formed after 1.5 h stirring. Then, the mixture was transferred into a 100 mL Teflon-lined autoclave. The autoclave was sealed and kept at 160 °C for 12 h, and then cooled to room temperature naturally. Finally, after being filtrated and washed with distilled water and absolute ethanol for several times and dried at 80 °C for 4 h, the product $Zn_mIn_2S_{m+3}@In_2S_3$ was obtained and named as ZIS/IS-J.

For comparison, pure $ZnIn_2S_4$ was prepared by the same procedures as above without adding $H_2C_2O_4 \cdot 2H_2O$ and denoted as ZIS-0. Pure In_2S_3 was obtained by the above same method using only $In_2(SO_4)_3 \cdot 6H_2O$ (1.0 mmol) and TAA (3.6 mmol) as raw materials and the product was named as IS. A H-H type $ZnIn_2S_4@In_2S_3$ heterojunction photocatalyst was prepared by precipitating In_2S_3 on ZIS-0 as follows. Firstly, 0.20 g

of the as-prepared ZIS-0 was dispersed in 60 mL of distilled water. Next, 1.0 mL of 8.5×10^{-4} mol L^{-1} $In_2(SO_4)_3$ aqueous solution and 1.0 mL of 2.4×10^{-4} mol L^{-1} TAA solution was in turn dropwise added into the dispersion of ZIS-0 under stirring. The molar ratio of In_2S_3 to $ZnIn_2S_4$ is 0.05. After 5 min ultrasonic dispersion, the mixture was heated to 90 °C and kept for 3 h under stirring. Finally, the product was separated by centrifugation, washed in turn with distilled water, ethanol, and then dried at 80 °C. The obtained sample was denoted as ZIS/IS-H.

2.2. Characterization

X-ray diffraction (XRD) patterns of the prepared samples were obtained on an XD-2/3 polycrystalline diffractometer employing nickel-filtered $Cu K\alpha$ radiation with four times scanning for each sample. UV-vis diffuse reflectance absorption spectra were obtained on a Hitachi U-3310 spectrophotometer equipped with an integrating sphere accessory with $BaSO_4$ as a reference. The scanning electron microscopy (SEM) images were taken on a JEOL JSM 6701 F equipped with an energy dispersive spectroscopy (EDS). The transmission electron microscopy (TEM), high-resolution electron microscopy (HRTEM) and scanning transmission electron microscope (STEM) images were taken on a FEI Talos F200 S equipped with an EDS. The EDS-mapping of the samples was recorded in spot scan mode by using a nanoprobe with the spot size of $0.2 \sim 2$ nm.

2.3. Photocurrent tests

The photocurrent tests were conducted on a LK 98BII electrochemical workstation in a three electrode cell. A Pt and Ag-AgCl electrode were used as the counter and reference electrode, respectively. The working electrode was prepared as follows. First, an ITO conducting glass (1.0×3.0 cm) was ultrasonically cleaned using acetone, ethanol and water in turn. Next, 50 mg of IS, ZIS-0, ZIS/IS-H or ZIS/IS-J, one drop (about 40 μL) of Triton X-100, one drop of acetyl-lacetone and 1.0 mL of distilled water were mixed and ground for 30 min. Then, one drop of the slurry was loaded on the cleaned glass (the covering area: 1.0×1.0 cm) with a glass rod by sliding to the tape-covered edges. Finally, the film was dried at 180 °C for 2 h in an oven to obtain the working electrode. The electrolyte was 0.20 mol L^{-1} Na_2SO_4 aqueous solution containing 0.59 mol L^{-1} triethanolamine (TEOA). A 350 W Xe lamp was used as the light source with a cut-off filter glass to remove radiation below 420 nm.

2.4. Photocatalytic reaction

Photocatalytic reaction was conducted in a 180 mL Pyrex flask with a flat window for irradiation at room temperature. The light source was a 350 W Xe lamp equipped with a glass cutoff filter ($\lambda \geq 420$ nm), and the irradiation intensity was 70 mW cm^{-2} . 0.10 g of a photocatalyst and 100 mL of the aqueous solution which contained 0.59 mol L^{-1} TEOA, and $1.93 \times 10^{-3} \text{ mol L}^{-1}$ H_2PtCl_6 (the calculated Pt amount was 1.0 wt%) were added into the cell. Before irradiation, the resulting suspension was treated with sonication for 5 min, and then bubbled with N_2 through the reaction mixture for 30 min to remove oxygen completely. A silicone rubber septum was fixed at the top of the cell, and the intermittent sampling was conducted through the septum. During the irradiation, the photocatalyst was remained in suspension by magnetic stirring, and metal Pt was in-situ photodeposited on the photocatalyst. The amount of photocatalytic hydrogen evolution was determined on a gas chromatograph (Thermal conductivity detector, 13X molecular sieve column, N_2 as gas carrier). In the stability test for ZIS/IS-J, the catalyst after each 5 h irradiation run was recovered by centrifugation; the fresh aqueous TEOA solution was renewed and flushed with N_2 for 30 min for a new irradiation run.

The apparent quantum yields (AQYs) at different monochromatic incident lights were estimated by the following equation.

$$\text{AQY} [\%] = 2 \times \frac{\text{mole of hydrogen evolved}}{\text{mole of incident photon}} \times 100\% \quad (1)$$

The reaction conditions including the reactor were the same as those for the above photocatalytic reaction except using various monochromatic LED lamps (UVEC-4, Shenzhen LAMPLIC Science Co Ltd, China) with effective lighting area of 0.80 cm^2 .

3. Results and discussion

3.1. Performance of ZIS/IS-J

Fig. 1a shows XRD patterns of ZIS-0 and ZIS/IS-J prepared by the same procedures and reactants except oxalic acid. All the diffraction peaks of ZIS-0 (without oxalic acid) can be assigned to the hexagonal phase of ZnIn_2S_4 (JCPDS Card No. 65-2023, $a = 3.85 \text{ \AA}$ and $c = 24.68 \text{ \AA}$). The main peaks of ZIS/IS-J (with oxalic acid) show no notable difference from those of ZIS-0 except a small diffraction shoulder at 27.4° next to the (102) main reflection at 27.7° of hexagonal ZnIn_2S_4 phase. This could be owing to the presence of In_2S_3 , which is further confirmed by the EDS and TEM measurements described below. Due to the adding atomic ratio of Zn^{2+} and In^{3+} of $1 : 2$ (the stoichiometric ratio of ZnIn_2S_4) in the preparation procedure for ZIS/IS-J and the presence of In_2S_3 in the product, the main peaks can be ascribed to hexagonal phase of $\text{Zn}_m\text{In}_2\text{S}_{m+3}$ solid solution ($m > 1$) whose XRD patterns are similar to that of ZnIn_2S_4 [25,38]. Thus, ZIS-0 consists of pure hexagonal ZnIn_2S_4 , whereas ZIS/IS-J comprises both hexagonal $\text{Zn}_m\text{In}_2\text{S}_{m+3}$ ($m > 1$) and In_2S_3 . However, the m value of the $\text{Zn}_m\text{In}_2\text{S}_{m+3}$ in ZIS/IS-J is only slightly greater than 1 because the diffraction peak of In_2S_3 is relatively weak, that is, the $\text{Zn}_m\text{In}_2\text{S}_{m+3}$ can approximate to ZnIn_2S_4 .

As shown in Fig. 1b, the optical properties of ZIS-0 and ZIS/IS-J were evaluated by UV-vis diffuse reflectance absorption spectroscopy. The two samples can absorb visible light with steep absorption edges, indicating that their absorptions are relevant to the intrinsic band gap transition. The absorption edge of ZIS/IS-J shows a little red shift compared to that of ZIS-0, supporting the presence of In_2S_3 . Accordingly, the band gap energies (E_g) of ZIS-0 and ZIS/IS-J obtained from plots of $(\alpha h\nu)^2$ versus photon energy $h\nu$ (the inset) are 2.46 and 2.40 eV, respectively.

To investigate chemical state of the elements for ZIS/IS-J, the XPS analysis was carried out (Fig. S1). The survey XPS spectrum of the sample indicates that the composite consists of S, In and Zn elements,

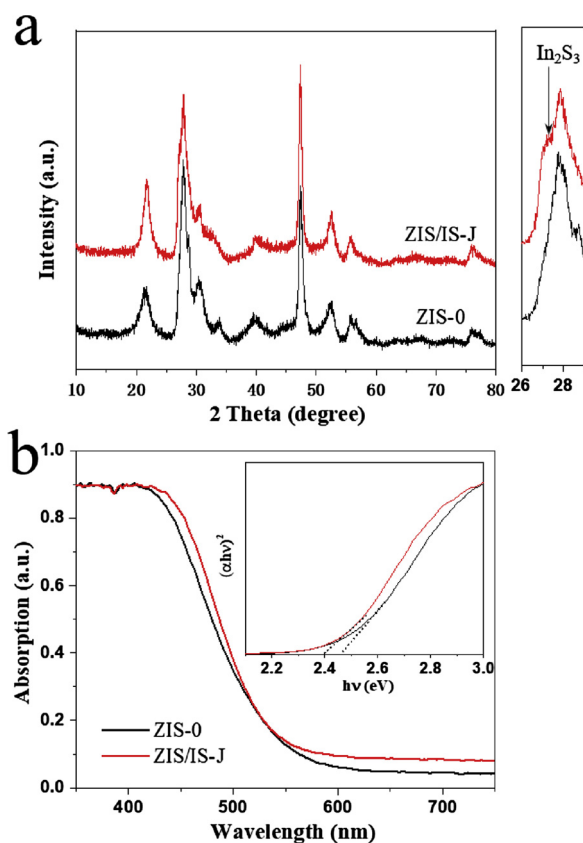


Fig. 1. (a) XRD patterns and (b) UV-vis diffuse reflectance absorption spectra of ZIS-0 and ZIS/IS-J. The inset of (b) is plots of $(\alpha h\nu)^2$ against photon energy ($h\nu$).

and no impurities can be observed except oxygen and carbon from the surface contamination. The peaks of $\text{Zn} 2p_{3/2}$, $\text{In} 3d_{5/2}$, and $\text{S} 2p_{3/2}$ are fixed at 1021.5, 445.3, and 162.3 eV, respectively (Fig. S1b–d). The spin orbit separations (Δ) of $\text{Zn}2p$, $\text{In}3d$, and $\text{S}2p$ are 23.1, 7.6, and 1.3 eV, respectively. These results show that the chemical states of the Zn, In and S elements are +2, +3 and -2, respectively [42,43].

The morphology of ZIS/IS-J was characterized via SEM and TEM/HRTEM. The sample consists of microspheres with the diameter of ca. $2.4 \sim 8.3 \text{ } \mu\text{m}$ (Fig. 2a). The inset of Fig. 2a shows clearly the hollow structure. Fig. 2b reveals that microspheres at a higher magnification exhibits ‘flower-like’ superstructure with numerous nano-petals. The TEM image confirms also that ZIS/IS-J is composed of microspheres (Fig. 2c). However, the hollow structure cannot be observed from TEM, which can be attributed to the fact that the hollow microspheres would be very large and thick. In order to confirm the hollow structure, ZIS/IS-J particles were embedded in an epoxy resin and microtomed into 70 nm thin sections. The SEM image of the section (Fig. S2) clearly indicates the hollow structure with the shell thickness of ca. 0.33–0.83 μm . Fig. 2d shows the HRTEM image of the out layer of a ZIS/IS-J microsphere. The front and side of nanosheets which correspond to ‘nano-petals’ of the SEM images, can be clearly observed.

To determine the location of In_2S_3 at ZIS/IS-J microspheres, ZIS/IS-J sample was characterized by EDS-mapping in spot scan mode. As shown in Fig. 3a–b, the rims of the nanosheets, that is, the positions 1 and 2, contain only In and S, indicating that the rims are composed of In_2S_3 . Furthermore, the side projection of a selective nanosheet was analyzed (positions 3–5). Fig. 3c shows that except the rim at position 2, the other parts (position 3–5) of the nanosheet comprise In, Zn and S simultaneously, namely $\text{Zn}_m\text{In}_2\text{S}_{m+3}$. The results confirm that In_2S_3 epitaxially grows along $\text{Zn}_m\text{In}_2\text{S}_{m+3}$ nanosheet rims to construct a J-J type $\text{Zn}_m\text{In}_2\text{S}_{m+3}@\text{In}_2\text{S}_3$ heterojunction. It is noted that the distance between position 2 and 3 is about 17 nm, suggesting that the length of

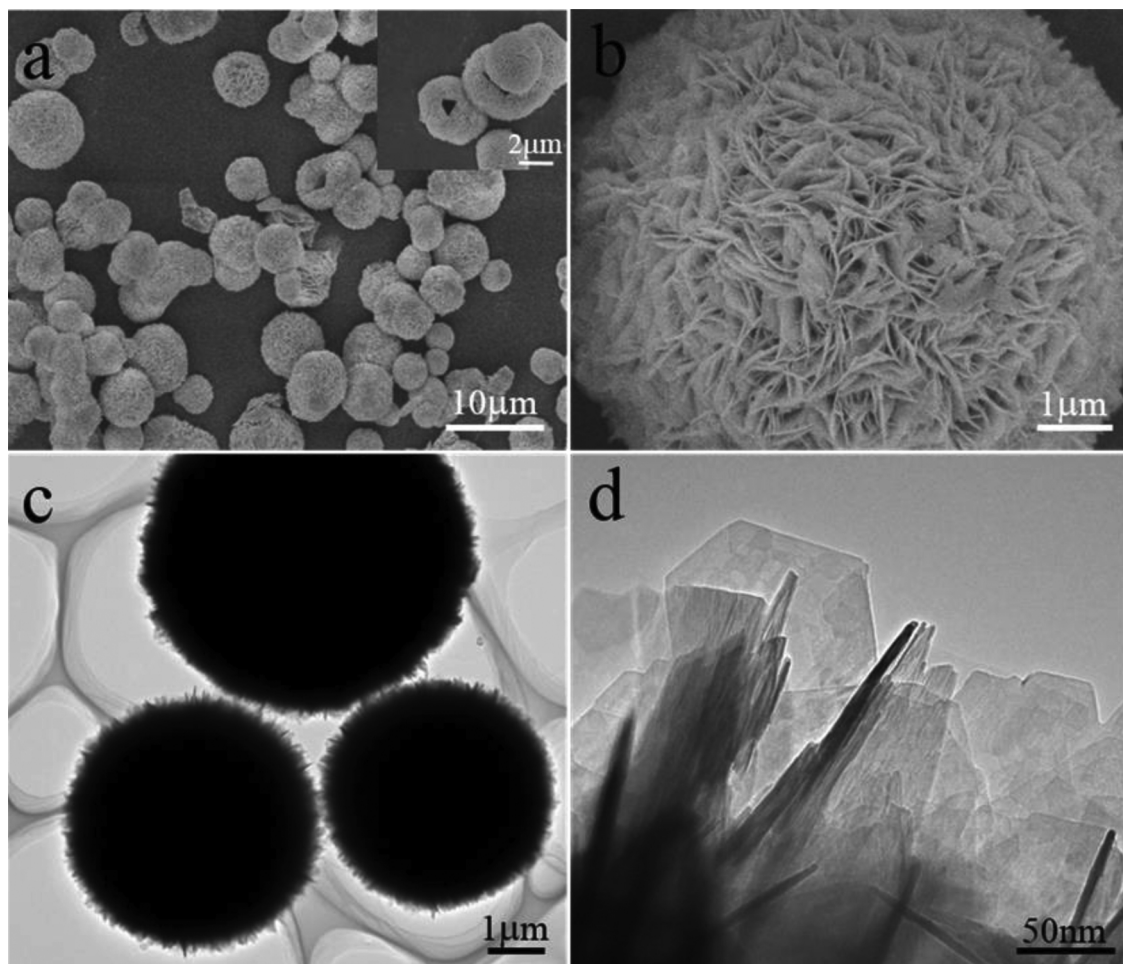


Fig. 2. (a) SEM image, (b) high magnification SEM image, (c) TEM image and (d) HRTEM image of ZIS/IS-J.

In_2S_3 nanosheet is less than 17 nm. Based on the above results, the hierarchical structure of a ZIS/IS-J microsphere is described by Fig. 3d. Owing to high thickness of $\text{Zn}_m\text{In}_2\text{S}_{m+3}$ hollow microspheres (Fig. S2) and short length of In_2S_3 nanosheets, the m value of the $\text{Zn}_m\text{In}_2\text{S}_{m+3}$ should be very close to 1. This is in agreement with the result from XRD (Fig. 1).

Fig. 4a illustrates the HRTEM image recorded along the rim of a ZIS/IS-J microsphere, which clearly shows an interface between $\text{Zn}_m\text{In}_2\text{S}_{m+3}$ and In_2S_3 , confirming also the J-J type heterogeneous structure. Both HRTEM and fast Fourier transformation (FFT) images for $\text{Zn}_m\text{In}_2\text{S}_{m+3}$ and In_2S_3 parts confirm that both $\text{Zn}_m\text{In}_2\text{S}_{m+3}$ and In_2S_3 parts form similar hexagonal structures with close unit cells and showing plate shape along (001) facet (Fig. 4b–c), and the In_2S_3 grows epitaxially along the (010)/(100) plane of $\text{Zn}_m\text{In}_2\text{S}_{m+3}$. The slightly larger d-spacing values for (100)/(010) planes in In_2S_3 than in $\text{Zn}_m\text{In}_2\text{S}_{m+3}$ are consistent with the composition contrast between $\text{Zn}_m\text{In}_2\text{S}_{m+3}$ and In_2S_3 . The diffraction doublets for each main reflection observed on the FFT image of $\text{Zn}_m\text{In}_2\text{S}_{m+3}$ (Fig. 4b) imply that the $\text{Zn}_m\text{In}_2\text{S}_{m+3}$ part in the rim of ZIS/IS-J microsphere could not be composed of single crystals. The intimate contact between the two parts is beneficial to charge transport and separation.

3.2. Photocatalytic performance

Fig. 5a gives the photocatalytic H_2 evolution activities of the as-synthesized IS (tetragonal In_2S_3 with $E_g = 2.03$ eV, Fig. S3), ZIS-0, ZIS/IS-J and ZIS/IS-H with 1.0 wt% Pt loaded by in situ photodeposited under visible light irradiation ($\lambda \geq 420$ nm). Very interestingly,

although the activity of single In_2S_3 is very low, when it couples with $\text{Zn}_m\text{In}_2\text{S}_{m+3}$ ($m \sim 1$) in J-J type, the activity of ZIS/IS-J ($330 \mu\text{mol h}^{-1}$) is about 4 times as high as that of single ZnIn_2S_4 (ZIS-0, $84 \mu\text{mol h}^{-1}$). However, H-H type $\text{ZnIn}_2\text{S}_4@\text{In}_2\text{S}_3$ (ZIS/IS-H, $79 \mu\text{mol h}^{-1}$) does not show the increased activity compared to ZIS-0. The activity of ZIS/IS-J notably surpasses that of the reported non-oriental $\text{ZnIn}_2\text{S}_4@\text{In}_2\text{S}_3$ heterojunction ($67.8 \mu\text{mol h}^{-1}$) [27]. The results indicate that the J-J type coupling of In_2S_3 plays a key role in the enhanced activity for ZIS/IS-J. The activity of ZIS/IS-J is 2.2 times as high as that of our recently reported J-type $\text{ZnIn}_2\text{S}_4@\text{In}(\text{OH})_3$ ($147 \mu\text{mol h}^{-1}$) [38], suggesting that In_2S_3 is an excellent sensitizer for $\text{ZnIn}_2\text{S}_4/\text{Zn}_m\text{In}_2\text{S}_{m+3}$. Moreover, the activity of ZIS/IS-J is much higher than those of the most reported ZnIn_2S_4 -based photocatalysts (Table S1).

To understand why ZIS/IS-J exhibits excellent photocatalytic activity for hydrogen evolution, photocurrent-time (I-t), photoluminescence (PL) and apparent quantum yield (AQY) measurement were carried out. As shown in Fig. 5b, the photocurrent order is ZIS/IS-J > ZIS/IS-H ~ ZIS-0 > IS, consistent with the activity order for the photocatalytic hydrogen evolution. This result confirms that the J-J type heterojunction can effectively separate and transfer the photo-generated carriers, whereas the H-H type one cannot. Generally, a material with a strong PL intensity implies its high charge recombination degree. ZIS-0, ZIS/IS-J and ZIS/IS-H (Fig. S4) show similar broad PL peaks at about 475 nm, and their emission intensities follow the following order: ZIS-0 ~ ZIS/IS-H > ZIS/IS-J, which also supports the above conclusion. Fig. 5c presents the apparent quantum yields (AQYs) of ZIS/IS-J, ZIS-0 and IS for photocatalytic hydrogen evolution at different incident light wavelengths. At 420 nm, both ZIS-0 and IS

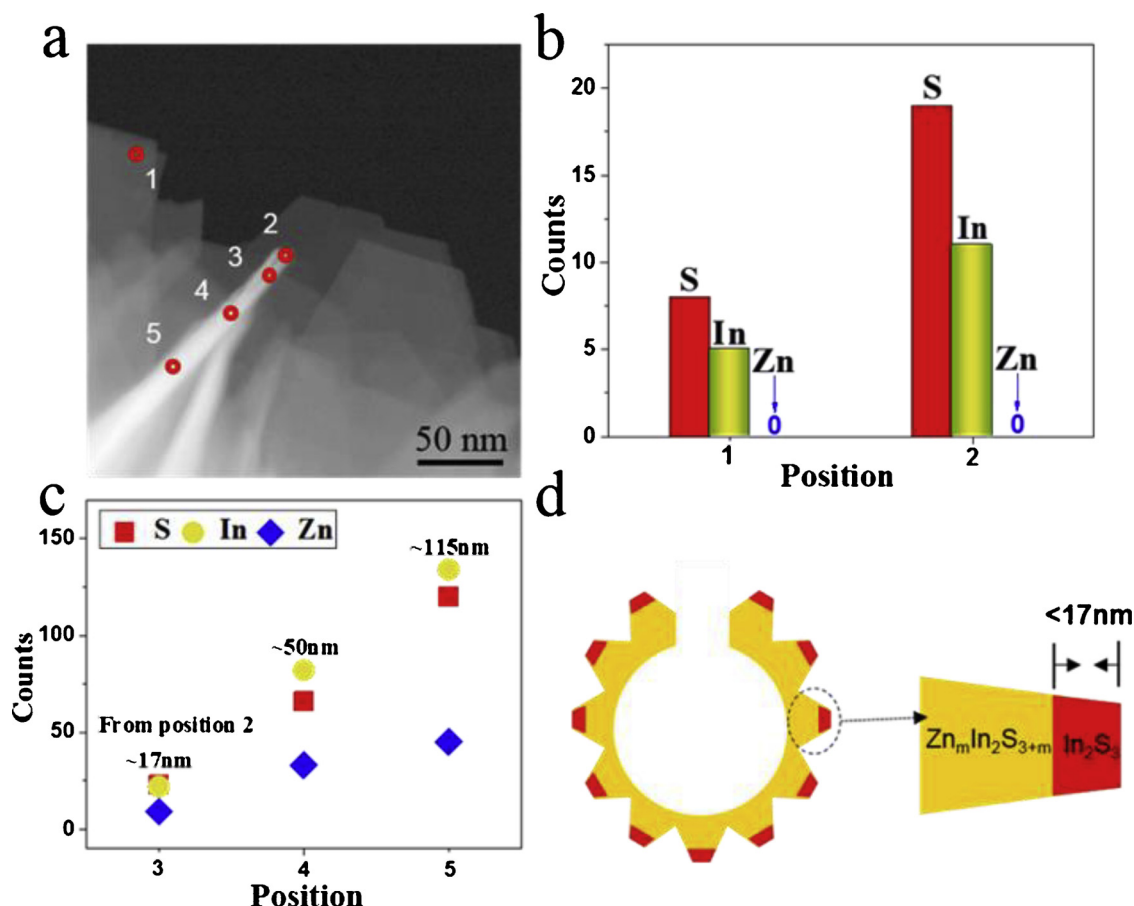


Fig. 3. (a) STEM image and (b, c) EDX analysis results at different positions of ZIS/IS-J nanosheets; (d) Schematic illustration of nanostructure of a ZIS/IS-J microsphere.

shows low AQY, whereas ZIS/IS-J exhibits much higher AQY than the sum of the both, further verifying that J-J type heterojunction has the excellent ability to transfer and separate the photogenerated carriers. On the other hand, although both ZIS-0 and IS display very low or no activity at 470, 520 and 545 nm, ZIS/IS-J shows remarkably enhanced activity, confirming that In_2S_3 effectively sensitizes $Zn_mIn_2S_{m+3}$ ($m \sim$

1) at long wavelengths. This indicates the potential of ZIS/IS-J for practical photocatalytic H_2 production with sunlight. This may be the main reason why ZIS/IS-J shows much higher activity than the reported J-type $ZnIn_2S_4@In(OH)_3$ [38].

Without loading Pt, the photocatalytic activities of IS, ZIS-0, ZIS/IS-H and ZIS/IS-J are 0, 6.1, 6.4 and $21 \mu\text{mol h}^{-1}$ (Fig. S5), respectively,

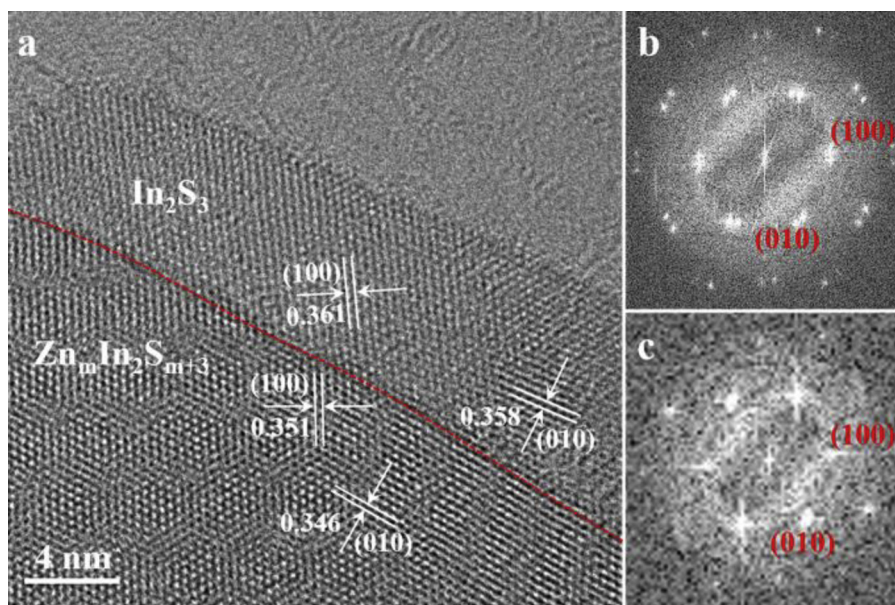


Fig. 4. (a) A typical HRTEM image recorded along the rim of a ZIS/IS-J microsphere with the FFT images for (b) $Zn_mIn_2S_{m+3}$ and (c) In_2S_3 parts. The red dash line represents the boundary between $Zn_mIn_2S_{m+3}$ and In_2S_3 (For interpretation of the references to colour in this figure legend, the reader is referred to the web version of this article).

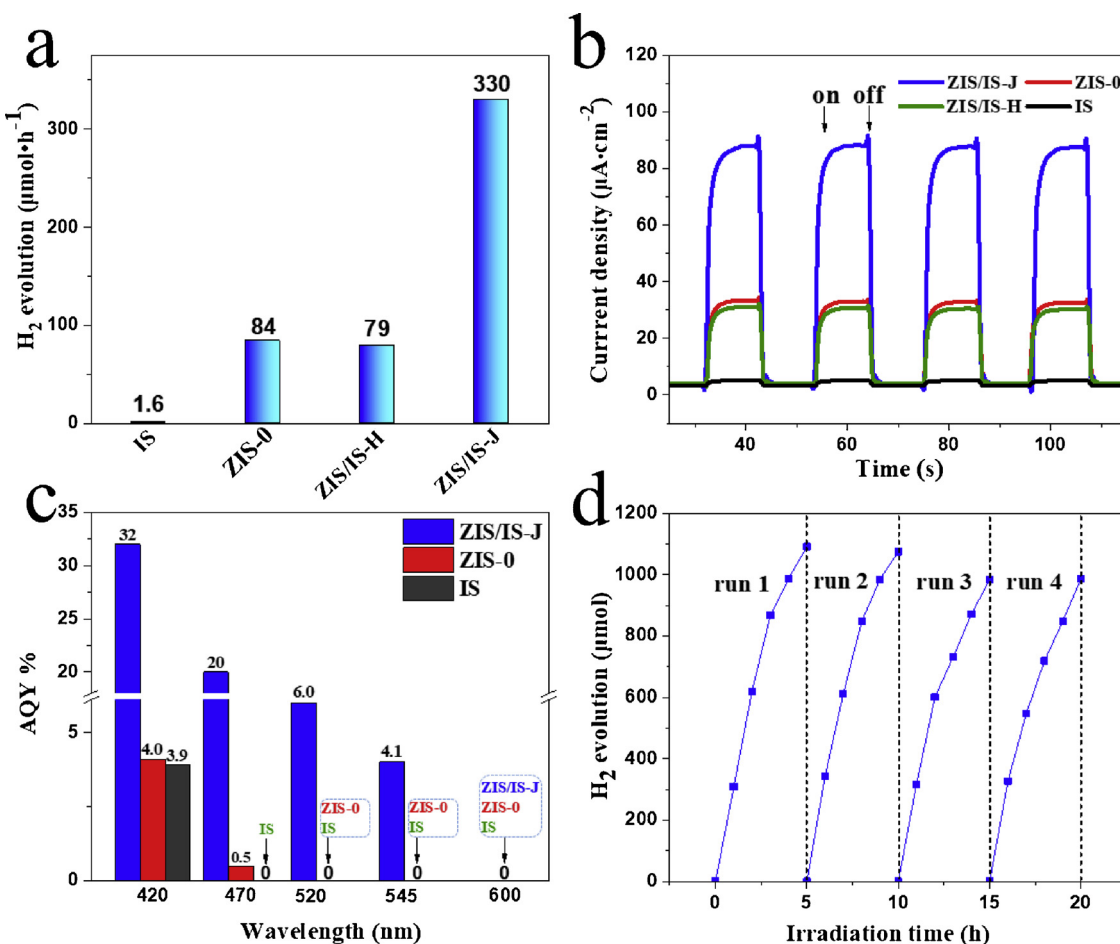


Fig. 5. (a) Photocatalytic activities of four samples with in situ depositing Pt; (b) Curves of transient photocurrent vs. irradiation time; (c) AQYs of ZIS/IS-J, IS and ZIS-0 with in situ depositing Pt at different incident light wavelengths; (d) Time curves of photocatalytic H_2 evolution over ZIS/IS-J with in situ depositing Pt.

much lower than those with loading 1.0 wt% Pt and displaying the same activity order as that with loading Pt. This result indicates that the in situ depositing Pt greatly improves the photocatalytic hydrogen evolution, and further confirms that ZIS/IS-J exhibits significantly higher carrier separation efficiency than ZIS/IS-H.

Good reusability is an important performance for an excellent photocatalyst. The photostability of ZIS/IS-J was investigated in four consecutive runs for 20 h irradiation by renewing the sacrificial reagent (TEOA) solution (Fig. 5d). After four runs, no obvious deactivation in photocatalytic H_2 evolution activity is observed. Moreover, the XRD pattern of ZIS/IS-J after the 4 photocatalytic runs still preserves its original integrity (Fig. S6). These results suggest the good stability of ZIS/IS-J.

3.3. Growth mechanism of ZIS/IS-J

When $H_2C_2O_4\cdot2H_2O$ was dissolved into the mixed solution of Zn^{2+} and In^{3+} ions in the preparation process, a white precipitate was produced which is mainly composed of monoclinic $In_2(C_2O_4)_3\cdot6H_2O$ (Detail discussion is given in the supplementary information and Fig. S7). The formed precipitate can act as heterogeneous nucleation centers to improve the growth of $Zn_mIn_2S_{3+m}$, leading to the formation of the hollow structure (Fig. S8). As $Zn_mIn_2S_{3+m}$ grew for a long time, for the metal ions, only In^{3+} ions left in the reaction system. Because the homogeneous nucleation of In_2S_3 is much more difficult than heterogeneous one at low concentration of free In^{3+} , the formed $Zn_mIn_2S_{3+m}/ZnIn_2S_4$ nanosheets (nano-petals) of the microspheres act as heterogeneous nucleation centers. Since $Zn_mIn_2S_{3+m}$ and $ZnIn_2S_4$ nanosheets

possess stable (001) exposed facet [38], the (100) and (010) facets perpendicular to the plane should be higher energy facets than (001) one. Thus, as shown in Figs. 3 and 4, at the extremely low supersaturation, the formed In_2S_3 monomers could epitaxially grow along the nanosheets to construct J-J type $Zn_mIn_2S_{3+m}@In_2S_3$ heterojunctions. The hexagonal In_2S_3 phase was reported as a high temperature phase [44]. Very interestingly, here the epitaxial growth along the (010)/(100) facet of layered hexagonal $Zn_mIn_2S_{3+m}$ stabilized the high-temperature hexagonal In_2S_3 phase under the hydrothermal environment.

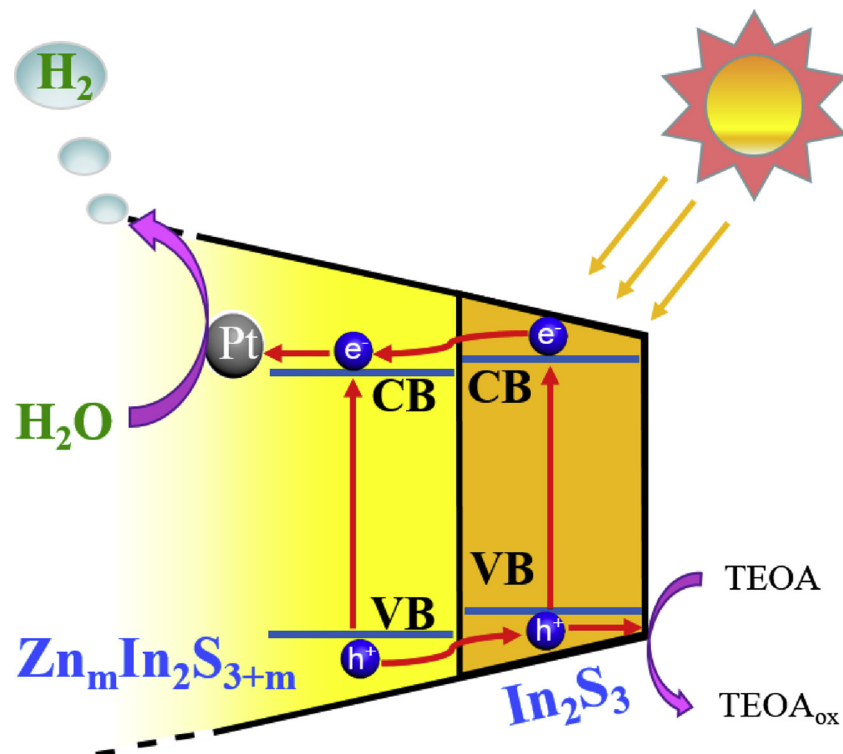
3.4. Mechanism of enhanced photoactivity of ZIS/IS-J

Because the m value of the as-prepared J-J type $Zn_mIn_2S_{3+m}@In_2S_3$ is only slightly greater than 1 (Figs. 1 and 3), we could assume that the values for the E_g and conduction band edge of $Zn_mIn_2S_{3+m}$ approximatively equal those of $ZnIn_2S_4$. However, the E_g value of the epitaxial In_2S_3 nanosheet of ZIS/IS-J (< 17 nm) should be much larger than bulk one (2.03 eV, Fig. S3) due to significant quantum confinement effect compared to the Bohr exciton radius of bulk In_2S_3 (33.8 nm) [45]. Based on the fact that E_g of ZIS/IS-J is 2.40 eV (Fig. 1b), E_g of the In_2S_3 nanosheet should roughly be equivalent to the value, consistent with the reported values in ref. 45.

The conduction band edge potential (E_{CB}) of a semiconductor can be estimated by the following equation [27, 46]:

$$E_{CB} = X - 1/2E_g - E^c \quad (2)$$

Where X and E_g are the absolute electronegativity and band gap energy of the semiconductor, respectively; E^c is the energy of free electrons on



Scheme 2. Proposed mechanism for photocatalytic hydrogen evolution over ZIS/IS-J with in situ photodeposited Pt.

the hydrogen scale (about 4.5 eV). According to the above equation, the conduction band (CB) edges of the In_2S_3 nanosheet ($E_g = 2.40$ eV) and $\text{Zn}_m\text{In}_2\text{S}_{m+3}/\text{ZnIn}_2\text{S}_4$ ($E_g = 2.46$ eV) are determined to be -1.0 and -0.836 V vs. NHE, respectively. Correspondingly, their valance band (VB) edges are 1.40 (In_2S_3 nanosheet) and 1.62 V ($\text{Zn}_m\text{In}_2\text{S}_{m+3}$) vs. NHE, respectively. The CB edges of IS and ZIS-0 obtained by Mott-Schottky plots are -0.99 and -0.84 V vs. NHE (Fig. S9), respectively, which are good agreement with the above estimated values. Thus, the photogenerated electron of the In_2S_3 nanosheet can transfer to CB of $\text{Zn}_m\text{In}_2\text{S}_{m+3}$, while the hole of $\text{Zn}_m\text{In}_2\text{S}_{m+3}$ to VB of In_2S_3 nanosheet, that is, a type II heterojunction (Scheme 2). Due to the formation of J-J type heterojunction, the carrier transfer and separation in/between the two semiconductors are highly efficient (Fig. 5b). This is the main reason for the high activity of ZIS/IS-J. Moreover, narrow In_2S_3 nanosheet shortens the diffusion path of photogenerated electron to $\text{Zn}_m\text{In}_2\text{S}_{m+3}$, which is the second reason for higher AQY of ZIS/IS-J at longer incident wavelengths (Fig. 5c). The In_2S_3 nanosheet ($E_g = 2.40$ eV) can absorb longer visible light than $\text{Zn}_m\text{In}_2\text{S}_{m+3}$, which is the third reason for the enhanced activity. Furthermore, the hollow structure and ‘flower-like’ superstructure not only enhances visible-light absorptivity and but also decreases the diffusion paths of reactants and products from the catalyst surface or bulk solution. As a result of the above four factors, ZIS/IS-J exhibits very high photocatalytic hydrogen evolution activity under visible light irradiation.

When ZIS/IS-J was irradiated by visible light, the photoexcited electrons and transferred electrons from In_2S_3 at CB of $\text{Zn}_m\text{In}_2\text{S}_{m+3}$ can reduce PtCl_6^{2-} into Pt. After the Pt deposition, the photoexcited and transferred electrons can be trapped by the deposited Pt to reduce water into H_2 . The holes are scavenged by the electron donor TEOA. Based on the above discussion, the proposed mechanism for the photocatalytic H_2 evolution over ZIS/IS-J with Pt as a cocatalyst under visible light irradiation is depicted as Scheme 2.

4. Conclusions

A novel J-J type $\text{Zn}_m\text{In}_2\text{S}_{m+3}/\text{In}_2\text{S}_3$ heterojunction photocatalyst

with hierarchical structures (hollow microspheres with flower-like superstructure) has been successfully fabricated with the assistance of oxalic acid. As the ligand, precipitant, provider of protons and template, oxalic acid decreases the supersaturation of $\text{Zn}_m\text{In}_2\text{S}_{m+3}$ and In_2S_3 , leading to the formation of J-J type $\text{Zn}_m\text{In}_2\text{S}_{m+3}/\text{In}_2\text{S}_3$ heterojunction with hollow structure. The J-J type heterojunction not only significantly enhances the carrier transport and separation efficiency, but also expands light response range of $\text{Zn}_m\text{In}_2\text{S}_{m+3}$. Moreover, the hollow structure and superstructure can also enhance visible-light absorptivity and decrease diffusion paths of reactants and products. Thus, the photocatalyst exhibits highly efficient photocatalytic H_2 evolution under visible light irradiation. The findings provide new insights to construct efficient oriented heterojunctions for anisotropic semiconductors.

Acknowledgements

This work was supported by the National Natural Science Foundation of China (Nos. 21563019, 21563020, 21703095), the Nature Science Foundation of the Jiangxi Province (No. 2017BAB206010). We thank Prof. Jing Ju and Mr. Wenda Zhang from College of Chemistry and Molecular Engineering, Peking University, for the STEM characterization.

Appendix A. Supplementary data

Supplementary material related to this article can be found, in the online version, at doi:<https://doi.org/10.1016/j.apcatb.2018.11.088>.

References

- [1] X.B. Chen, S.H. Shen, L.J. Guo, S.S. Mao, Semiconductor-based photocatalytic hydrogen generation, *Chem. Rev.* 110 (2010) 6503–6570.
- [2] J.Y. Xu, Y.X. Li, S.Q. Peng, G.X. Lu, S.B. Li, Eosin Y-sensitized graphitic carbon nitride fabricated by heating urea for visible light photocatalytic hydrogen evolution: the effect of the pyrolysis temperature of urea, *Phys. Chem. Chem. Phys.* 15 (2013) 7657–7665.

[3] Y.X. Li, H. Wang, S.Q. Peng, Tunable photodeposition of MoS₂ onto a composite of reduced graphene oxide and CdS for synergic photocatalytic hydrogen generation, *J. Phys. Chem. C* 118 (2014) 19842–19848.

[4] Y. Ma, X.L. Wang, Y.S. Jia, X.B. Chen, H.X. Han, C. Li, Titanium dioxide-based nanomaterials for photocatalytic fuel generations, *Chem. Rev.* 114 (2014) 9987–10043.

[5] W.Y. Zhang, Y.X. Li, S.Q. Peng, Template-free synthesis of hollow Ni/reduced graphene oxide composite for efficient H₂ evolution, *J. Mater. Chem. A* 5 (2017) 13072–13078.

[6] W.Y. Zhang, Y.X. Li, S.Q. Peng, Facile synthesis of graphene sponge from graphene oxide for efficient dye-sensitized H₂ evolution, *ACS Appl. Mater. Interfaces* 8 (2016) 15187–15195.

[7] W.Y. Zhang, Y.X. Li, X.P. Zeng, S.Q. Peng, Synergistic effect of metal nickel and graphene as a cocatalyst for enhanced photocatalytic hydrogen evolution via dye sensitization, *Sci. Rep.* 5 (2015) 10589.

[8] Y.X. Li, C.F. Xie, S.Q. Peng, G.X. Lu, S.B. Li, Eosin Y-sensitized nitrogen-doped TiO₂ for efficient visible light photocatalytic hydrogen evolution, *J. Mol. Catal. A Chem.* 282 (2008) 117–123.

[9] Y.X. Li, K. Zhang, S.Q. Peng, G.X. Lu, S.B. Li, Photocatalytic hydrogen generation in the presence of ethanolamines over Pt/ZnIn₂S₄ under visible light irradiation, *J. Mol. Catal. A Chem.* 363–364 (2012) 354–361.

[10] Y.X. Li, D. Gao, S.Q. Peng, G.X. Lu, S.B. Li, Photocatalytic hydrogen evolution over Pt/Cd_{0.5}Zn_{0.5}S from saltwater using glucose as electron donor: an investigation of the influence of electrolyte NaCl, *Int. J. Hydrogen Energy* 36 (2011) 4291–4297.

[11] Y.X. Li, G.X. Lu, S.B. Li, Photocatalytic production of hydrogen in single component and mixture systems of electron donors and monitoring adsorption of donors by in situ infrared spectroscopy, *Chemosphere* 52 (2003) 843–850.

[12] Y.X. Li, G.X. Lu, S.B. Li, Photocatalytic hydrogen generation and decomposition of oxalic acid over platinized TiO₂, *Appl. Catal. A* 214 (2001) 179–185.

[13] Z. Lei, W. You, M. Liu, G. Zhou, T. Takata, M. Hara, K. Domen, C. Li, Photocatalytic water reduction under visible light on a novel ZnIn₂S₄ catalyst synthesized by hydrothermal method, *Chem. Commun.* (2003) 2142–2143.

[14] B. Chai, T.Y. Peng, P. Zeng, X.H. Zhang, X.J. Liu, Template-free hydrothermal synthesis of ZnIn₂S₄ flowered microspheres as an efficient photocatalyst for H₂ production under visible-light irradiation, *J. Phys. Chem. C* 115 (2011) 6149–6155.

[15] S.H. Shen, L. Zhao, L.J. Guo, Cetyltrimethylammonium bromide (CTAB)-assisted hydrothermal synthesis of ZnIn₂S₄ as an efficient visible-light-driven photocatalyst for hydrogen production, *Int. J. Hydrogen Energy* 33 (2008) 4501–4510.

[16] L. Shang, C. Zhou, T. Bian, H.J. Yu, L.Z. Wu, C.H. Tung, T.R. Zhang, Facile synthesis of hierarchical ZnIn₂S₄ submicrospheres composed of ultrathin mesoporous nanosheets as a highly efficient visible-light-driven photocatalyst for H₂ production, *J. Mater. Chem. A* 1 (2013) 4552–4558.

[17] Z.D. Xu, Y.X. Li, S.Q. Peng, G.X. Lu, S.B. Li, NaCl-assisted low temperature synthesis of layered Zn-In-S photocatalyst with high visible-light activity for hydrogen evolution, *RSC Adv.* 2 (2012) 3458–3466.

[18] G.H. Tian, Y.J. Chen, Z.Y. Ren, C.G. Tian, K. Pan, W. Zhou, J.Q. Wang, H.G. Fu, Enhanced photocatalytic hydrogen evolution over hierarchical composites of ZnIn₂S₄ nanosheets grown on MoS₂ slices, *Chem. Asian J.* 9 (2014) 1291–1297.

[19] Y.X. Li, J.X. Wang, S.Q. Peng, G.X. Lu, S.B. Li, Photocatalytic hydrogen generation in the presence of glucose over ZnS-Coated ZnIn₂S₄ under visible light irradiation, *Int. J. Hydrogen Energy* 35 (2010) 7116–7126.

[20] S.Q. Peng, M. Ding, T. Yi, Y.X. Li, Photocatalytic hydrogen evolution in the presence of pollutant methylamines over Pt/ZnIn₂S₄ under visible light irradiation, *J. Mol. Catal. (China)* 28 (2014) 466–473.

[21] F. Tian, R.S. Zhu, K.L. Song, F. Ouyang, G. Cao, The effects of amount of La on the photocatalytic performance of ZnIn₂S₄ for hydrogen generation under visible light, *Int. J. Hydrogen Energy* 40 (2015) 2141–2148.

[22] Q. Li, C. Cui, H. Meng, J.G. Yu, Visible-light photocatalytic hydrogen production activity of ZnIn₂S₄ microspheres using carbon quantum dots and platinum as dual co-catalysts, *Chem. Asian J.* 9 (2014) 1766–1770.

[23] W.L. Yang, L. Zhang, J.F. Xie, X.D. Zhang, Q.H. Liu, T. Yao, S.Q. Wei, Q. Zhang, Y. Xie, Enhanced photoexcited carrier separation in oxygen-doped ZnIn₂S₄ nanosheets for hydrogen evolution, *Angew. Chem. Int. Ed.* 55 (2016) 6715–6719.

[24] G.P. Chen, N. Ding, F. Li, Y.Z. Fan, Y.H. Luo, D.M. Li, Q.B. Meng, Enhancement of photocatalytic H₂ evolution on ZnIn₂S₄ loaded with in-situ photo-deposited MoS₂ under visible light irradiation, *Appl. Catal. B: Environ.* 160–161 (2014) 614–620.

[25] S.H. Shen, L. Zhao, L.J. Guo, Zn_mIn₂S_{3+m} (m=1–5, integer): a new series of visible-light-driven photocatalysts for splitting water to hydrogen, *Int. J. Hydrogen Energy* 35 (2010) 10148–10154.

[26] A.V. Anagnostopoulos, C. Manolikas, D. Papadopoulos, J. Spyridel, Composition faults in ZnIn₂S₄ (III) layered crystals and their influence on the anisotropic conductivity of this compound, *Phys. Status Solidi A* 72 (1982) 731–736.

[27] Z.W. Mei, S.X. Ouyang, D.M. Tang, T. Kako, D. Golberg, J.H. Ye, An ion-exchange route for the synthesis of hierarchical In₂S₃/ZnIn₂S₄ bulk composite and its photocatalytic activity under visible-light irradiation, *Dalton Trans.* 42 (2013) 2687–2690.

[28] Q. Liu, H. Lu, Z.W. Shi, F.L. Wu, J. Guo, K.M. Deng, L. Li, 2D ZnIn₂S₄ nanosheet/1D TiO₂ nanorod heterostructure arrays for improved photoelectrochemical water splitting, *ACS Appl. Mater. Interfaces* 6 (2014) 17200–17207.

[29] Y.J. Chen, G.H. Tian, Z.Y. Ren, K. Pan, Y.H. Shi, J.Q. Wang, H.G. Fu, Hierarchical core–shell carbon nanofiber/ZnIn₂S₄ composites for enhanced hydrogen evolution performance, *Appl. Mater. Interfaces* 6 (2014) 13841–13849.

[30] Y.J. Chen, H. Ge, L. Wei, Z.H. Li, R.S. Yuan, P. Liu, X.Z. Fu, Reduction degree of reduced graphene oxide (RGO) dependence of photocatalytic hydrogen evolution performance over rGO/ZnIn₂S₄ nanocomposites, *Catal. Sci. Technol.* 3 (2013) 1712–1717.

[31] L. Ye, Z.H. Li, Rapid microwave-assisted syntheses of reduced graphene oxide (RGO)/ZnIn₂S₄ microspheres as superior noble-metal-free photocatalyst for hydrogen evolutions under visible light, *Appl. Catal. B: Environ.* 160–161 (2014) 552–557.

[32] N. Ding, Y.Z. Fan, Y.H. Luo, D.M. Li, Q.B. Meng, Enhancement of H₂ evolution over new ZnIn₂S₄/RGO/MoS₂ photocatalysts under visible light, *APL Mater.* 3 (2015).

[33] Y.J. Yuan, J.R. Tu, Z.J. Ye, D.Q. Chen, B. Hu, Y.W. Huang, T.T. Chen, D.P. Cao, Z.T. Yu, Z.G. Zou, MoS₂-graphene/ZnIn₂S₄ hierarchical microarchitectures with an electron transport bridge between light-harvesting semiconductor and cocatalyst: a highly efficient photocatalyst for solar hydrogen generation, *Appl. Catal. B: Environ.* 188 (2016) 13–22.

[34] Z.Y. Zhang, K.C. Liu, A.Q. Feng, Y.N. Bao, B. Dong, Hierarchical sheet-on-Sheet ZnIn₂S₄/g-C₃N₄ heterostructure with highly efficient photocatalytic H₂ production based on photoinduced interfacial charge transfer, *Sci. Rep.* 6 (2016) 19221.

[35] X. Chen, L. Li, W.Z. Zhang, Y.X. Li, Q. Song, L. Dong, Fabricate globular flower-like Cu₃CdIn₂S₄/ZnIn₂S₄ with high visible light response via microwave-assisted one-step method and its multipathway photoelectron migration properties for hydrogen evolution and pollutant degradation, *ACS Sustain. Chem. Eng.* 4 (2016) 6680–6688.

[36] H. Liu, J. Zhang, D. Ao, Construction of heterostructured ZnIn₂S₄@NH₂-MIL-125(Ti) nanocomposites for visible-light-driven H₂ production, *Appl. Catal. B: Environ.* 221 (2018) 433–442.

[37] L.K. Gallos, A.N. Anagnostopoulos, P. Argyrakis, Conduction anisotropy in layered semiconductors, *Phys. Rev. B* 50 (1994) 14643–14646.

[38] Y.X. Li, Y.L. Hou, Q.Y. Fu, S.Q. Peng, Y.H. Hu, Oriented growth of ZnIn₂S₄/In(OH)₃ heterojunction by a facile hydrothermal transformation for efficient photocatalytic H₂ production, *Appl. Catal. B: Environ.* 206 (2017) 726–733.

[39] X.L. Fu, X.X. Wang, Z.X. Chen, Z.Z. Zhang, Z.H. Li, D.Y. Leung, L. Wu, Photocatalytic performance of tetragonal and cubic β-In₂S₃ for the water splitting under visible light irradiation, *Appl. Catal. B: Environ.* 95 (2010) 393–399.

[40] Y. Sharma, P. Srivastava, Electronic, optical and transport properties of α-, β- and γ-phases of spinel indium sulphide: An ab initio study, *Mater. Chem. Phys.* 135 (2012) 385–394.

[41] C.N.R. Rao, S. Natarajan, R. Vaidhyanathan, Metal carboxylates with open architectures, *Angew. Chem. Int. Ed.* 43 (2004) 1466–1496.

[42] M. Hojamberdiev, Y. Cai, J.J.M. Vequizo, M.M. Khan, R. Vargas, K. Yubuta, M. Hasegawa, Binary flux-promoted formation of trigonal ZnIn₂S₄ layered crystals using ZnS-containing industrial waste and their photocatalytic performance for H₂ production, *Green Chem.* 20 (2018) 3845–3856.

[43] Z.X. Chen, D.Z. Li, W.J. Zhang, C. Chen, W.J. Li, M. Sun, Y.H. He, X.Z. Fu, Low-temperature and template-free synthesis of ZnIn₂S₄ microspheres, *Inorg. Chem.* 47 (2008) 9766–9772.

[44] K.D. Kundra, S.Z. Ali, X-ray study of thermal expansion and phase transformation in β-In₂S₃, *Phys. Status Solidi* 36 (1976) 517–525.

[45] R.K. Sharma, Y.N. Chouryal, S. Chaudhari, J. Saravanakumar, S.R. Dey, P. Ghosh, Adsorption-driven catalytic and photocatalytic activity of phase tuned In₂S₃ nanocrystals synthesized via ionic liquids, *ACS Appl. Mater. Interfaces* 9 (2017) 11651–11661.

[46] Y. Xu, M.A.A. Schoonen, The absolute energy positions of conduction and valence bands of selected semiconducting minerals, *Am. Mineral.* 85 (2000) 543–556.